

---

# Methods to project plasticity models onto the contact surface applied to soil structure interactions

C. Weißenfels · P. Wriggers

**Abstract** In this work two new concepts for a direct application of plasticity models within a frictional contact description are developed. These concepts can be used in conjunction with all different kinds of contact formulations and solution methods. Additionally, all types of plasticity models can be projected onto the contact surface. The advantage of these concepts is shown exemplary in the modeling process of soil-structure interactions where the projected plasticity models are able to describe the soil behavior at the contact surface. The numerical implementation of the new frictional relations is based on the Mortar method. A new type of mixed formulation is also introduced combining the augmented Lagrangian method to enforce the normal contact constraint with the penalty regularization written in Hellinger-Reissner form to implement the tangential contact behavior. This reformulation leads to a reduction of the CPU time compared to the standard penalty regularization, if the Mortar method is used. Finally, the numerical investigation of a direct shear test shows the accurate reproduction of the typical stress-strain relation of the soil at the contact surface.

**Keywords** Contact Mechanics · Finite element method · Mortar method · Friction laws · Projection strategies · Soil mechanics · Soil-structure interactions

## 1 Introduction

When investigating simulations of sliding contacts, Coulomb's law is mostly preferred to model the frictional behavior. Even within the highly complex modeling process of soil-structure interactions Coulomb's law is applied [1],[2], although the simulation of a pile penetration process shows a large difference between numerical and experimental results (figure 1,[3]). As a consequence new frictional models were developed in [3] improving the slip behavior. Unfortunately, a large number of additional material parameters was introduced there which have to be determined for each individual contact pair.

---

C. Weißenfels (✉)

Institute of Continuum Mechanics, Leibniz University of Hannover, Appelstr. 11, 30167 Hannover, Germany  
E-mail: weissenfels@ikm.uni-hannover.de

P. Wriggers

Institute of Continuum Mechanics, Leibniz University of Hannover, Appelstr. 11, 30167 Hannover, Germany  
E-mail: wriggers@ikm.uni-hannover.de

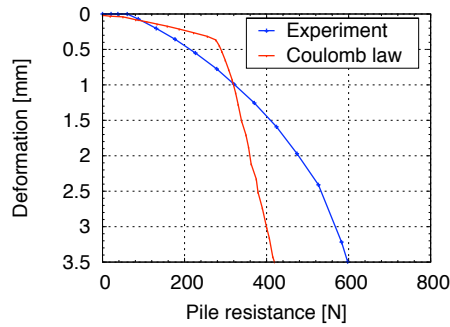


Figure 1: Comparison of experimental and numerical results of a pile penetration test [3]

Within geotechnical installation processes for piles, anchors or sheet pile walls, mostly the surface of the structure has to be viewed as rough. Experimental measurements of a direct shear test between soil and concrete show that for a rough surface of the structure the response behavior is almost equal to the same test case between two soil specimens [4],[5],[6]. This causes the assumption that for these soil-structure interactions the real contact zone lies completely within the soil (figure 2). Since many soil

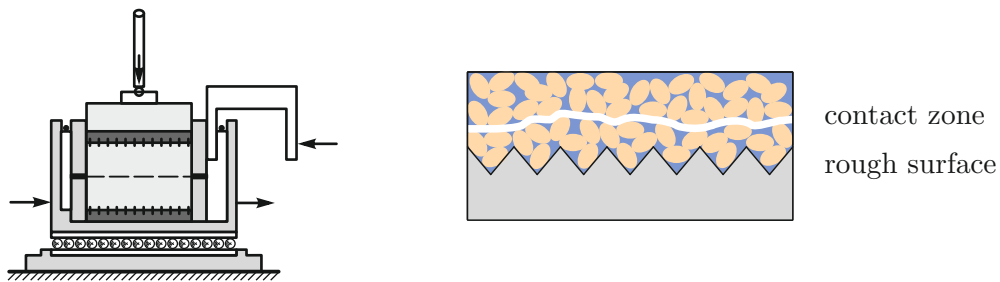


Figure 2: Development of the contact zone in a direct shear test between a soil and a concrete specimen with a rough surface

models are able to represent the 3-dimensional geomechanical behavior exactly, the description of the mechanics at the contact layer can be improved by the use of such models. Until now either interface elements [7], [8], or special joint elements [9], [10] are used to model the contact interface by use of soil models. Additionally, some interface models exist where the rough surface structure is taken into account [11], [12]. These models are limited to small sliding and only an incorporation into contact formulations makes it possible to simulate more realistic situations where large relative movements occur, like pile installation processes for instance. Hence within this work two different strategies are developed each able to incorporate the plasticity models directly into a friction model. Another advantage of this projection schemes is that no additional parameters are needed.

A big challenge of any projection method, especially for soil-structure interactions, is the correct reproduction of the dilatant or contractant behavior at the contact surface. A direct integration of these influences into a contact model would lead in the case of contractancy to a penetration of one body into the other which is not allowed or in the case of dilatancy to a release of the contact during the

sliding process which is not reasonable. Additionally, yield criteria are often formulated in terms of three stress invariants whereas slip laws are mostly based on the norm of the tangential stress vector and on the absolute value of the normal pressure. Hence a direct link between these invariants is not possible. However in the literature some relation between contact and continuum are disclosed. For instance, the 3-dimensional Mohr-Coulomb yield criterion is the natural extension of the two dimensional Coulomb slip rule [13]. Using the penalty regularization for the tangential contact a formulation analog to the elasto-plastic theory can be exploited in the modeling process [14],[15],[16]. Both relations are providing the basis for the developed projection methods.

If the surface of the structure can be assumed as perfectly smooth, contact takes place directly at the interface of soil and structure and Coulomb's law can be used, as can be seen in the outcomes of experimental tests between steel and soil in [17] or [18]. Only a proper coefficient of friction has to be determined.

For the numerical implementation of the new friction models first the boundary value problem has to be described. The discretization of the leading equations within a finite element framework is displayed in section 2 where the focus lies especially on the contact part. In this work the Mortar method [19] is used exemplary for the discretization of the contact part leading to a robust solution algorithm [20]. A new type of mixed version is embedded in the Mortar framework which combines the augmented Lagrangian method [21],[22] for the normal contact description with the penalty regularization given in Hellinger-Reissner form for the tangential part delivering a stable solution technique for contact models.

A soil model based on the framework of the elasto-plastic theory which is able to include the porous structure of the soil [23],[24] is stated in section 3. Additionally, two regularization schemes are mentioned shortly at the end of this section which stabilize the back-projection within the return mapping algorithm and avoid oscillations between the elastic and plastic state of a material point.

Section 4 and 5 describe the two developed projection methods in detail. The first one transforms the plasticity equations properly into frictional formulations using the connection between Coulomb slip rule and Mohr-Coulomb yield criterion. The second concept integrates the plasticity model directly into the slip rule formulating a continuum stress dependent coefficient of friction and normal contact force. The results of the new projection concepts are shown at the end of each section within numerical investigations of a direct shear test. There the outcomes are compared with the results of a corresponding 3-dimensional setup using interface elements in between of the two contact specimens. The presented work is closed with an evaluation of both projection schemes in section 6.

## 2 A mixed Mortar method

The new friction models can be solved with all kinds of contact formulations. In this work the new contact equations are included into a solution method that is embedded in a Mortar framework. To have a natural transformation from plasticity to friction and additionally a strong enforcement of the non penetration condition a new type of mixed formulation is proposed. There the normal contact constraint is solved using the augmented Lagrangian method and the tangential constraint is regularized with the penalty method written in Hellinger-Reissner form.

### 2.1 Boundary value problem

In the following investigations only quasi-static cases will be considered that rely on constitutive models for small strain applications. Additionally, the influence of the gravity force is neglected to concentrate

on the pressure dependency of the numerical response behavior. The balance equation of momentum for each contacting body simplifies then to the requirement that the divergence of each stress  $\boldsymbol{\sigma}^i$  has to be zero

$$\operatorname{div} \boldsymbol{\sigma}^i = 0 \quad \text{in } B^i. \quad (1)$$

Here index (i=1) stands for the body which surface will be denoted as slave surface and (i=2) denotes the master surface. This distinction was introduced in [25]. The boundary of each body is subdivided into the Neumann boundary where the applied traction  $\bar{\mathbf{t}}^i$  is given and into the Dirichlet boundary where the applied displacements  $\bar{\mathbf{u}}^i$  are prescribed

$$\begin{aligned} \boldsymbol{\sigma}^i \mathbf{n}^i &= \bar{\mathbf{t}}^i & \text{on } & \partial_\sigma B^i \\ \mathbf{u}^i &= \bar{\mathbf{u}}^i & \text{on } & \partial_u B^i. \end{aligned} \quad (2)$$

In the case of contact a third boundary part  $\partial_c B$  has to be considered which denotes the contact area. Hence the boundary of each body is uniquely subdivided in three different regions  $\partial_\sigma B^i \cap \partial_u B^i \cap \partial_c B = \emptyset$ . On the contact boundary the normal gap

$$g_N = (\mathbf{x}^2 - \mathbf{x}^1) \cdot \mathbf{n}^1 \quad (3)$$

and the pressure  $\lambda_N$  determines the contact behavior in normal direction. For the computation of  $g_N$  the actual position vectors  $\mathbf{x}^i$  of the master and of the slave surface are used, see also [16]. Contact takes place, if the normal penetration is equal to zero. In the case of non touching bodies the contact pressure has to vanish leading to the set of inequalities which can also be written in the Karush-Kuhn-Tucker form

$$g_N \geq 0, \quad \lambda_N \leq 0, \quad g_N \lambda_N = 0 \quad \text{on } \partial_c B. \quad (4)$$

Similarly, for the tangential contact two inequalities can be stated to define the stick or the slip state of the surface point. Thereby friction takes place, if the slip rule  $f^c$  is equal to zero introducing additionally a slip rate ( $\dot{\gamma} > 0$ ). In analogy to the elasto-plastic theory, an evolution equation for the tangential gap  $\mathbf{g}_T$  is defined where the direction of sliding corresponds to the direction of the tangential contact stress vector  $\boldsymbol{\lambda}_T$

$$\begin{aligned} \dot{\gamma} \geq 0, \quad f^c(\|\boldsymbol{\lambda}_T\|, \lambda_N) \leq 0, \quad \dot{\gamma} f^c = 0 & \quad \text{on } \partial_c B \\ \dot{\mathbf{g}}_T = \dot{\gamma} \frac{\boldsymbol{\lambda}_T}{\|\boldsymbol{\lambda}_T\|}. \end{aligned} \quad (5)$$

A detailed derivation and explanation of the mentioned equations can be found for instance in standard contact textbooks [16],[26].

## 2.2 Finite element discretization

For the solution of contact problems the finite element method is often employed. For this, first the balance of momentum (1) of each body together with the normal (4) and tangential contact constraints (5) has to be written in a weak form

$$\sum_{i=1}^2 G^i(\mathbf{u}, \boldsymbol{\eta}) + G_u^c(\mathbf{u}, \boldsymbol{\eta}, \boldsymbol{\lambda}) + G_l^c(\mathbf{u}, \boldsymbol{\eta}, \delta \boldsymbol{\lambda}) = 0. \quad (6)$$

The formulation and discretization of the virtual work part of the two contacting bodies  $G^i(\mathbf{u}, \boldsymbol{\eta})$  can be found in standard finite element textbooks, like [27],[28] and will not be specified explicitly. For the

proposed mixed formulation of the contact part the weak form is split into the contact virtual work  $G_u^c(\mathbf{u}, \boldsymbol{\eta}, \boldsymbol{\lambda})$  and into the formulation of the contact constraints  $G_l^c(\mathbf{u}, \boldsymbol{\eta}, \delta\boldsymbol{\lambda})$ . Like for the augmented Lagrangian or pure Lagrange multiplier method, in this description the contact stress vector is introduced as an additional unknown  $\boldsymbol{\lambda}$ . Contrary to the formulations in [29],[30],[31] in the virtual contact work part the Lagrange multiplier  $\boldsymbol{\lambda}$  is subdivided into the normal  $\lambda_N$  and the tangential stress components  $\lambda_{T\alpha}$

$$G_u^c(\mathbf{u}, \boldsymbol{\eta}, \boldsymbol{\lambda}) = \int_{\partial B_c} \delta g_N \lambda_N \, da + \int_{\partial B_c} \delta g_{T\alpha} \lambda_{T\alpha} \, da \quad (7)$$

leading to a symmetric tangent in the case of stick. The weak form of the contact constraints  $G_l^c(\mathbf{u}, \boldsymbol{\eta}, \delta\boldsymbol{\lambda})$  is further subdivided into a normal and a tangential part. In the mixed method the augmented Lagrangian [21] or sometimes called primal dual method [22] is applied to fulfill the normal constraint. Using a nonlinear complementarity function, like in [22], the weak normal contact constraint can be reformulated as

$$G_{l_N}^c(\mathbf{u}, \boldsymbol{\eta}, \boldsymbol{\lambda}) = \int_{\partial B_c} \delta\lambda_N \frac{1}{c_N} [\lambda_N - \min\{\lambda_N + c_N g_N, 0\}] \, da = 0. \quad (8)$$

Contrary to [22] the equation is weighted with the inverse of the penalty parameter to be consistent with the units. The minimum function is also used instead of the maximum function [22], since in this work the contact pressure has a negative sign. Depending on the minimum function the weak form either forces the normal penetration or the normal Lagrange multiplier to be equal to zero leading to the distinction

$$\begin{aligned} \text{active :} \quad & \lambda_N + c_N g_N \leq 0 \quad \rightarrow \quad G_{l_N}^c = \int_{\partial B_c} \delta\lambda_N g_N \, da = 0 \\ \text{inactive :} \quad & \lambda_N + c_N g_N > 0 \quad \rightarrow \quad G_{l_N}^c = \int_{\partial B_c} \delta\lambda_N \frac{1}{c_N} \lambda_N \, da = 0. \end{aligned} \quad (9)$$

Using the analogy to the elasto-plastic theory the penalty regularization is used to enforce the tangential contact constraint. In the Mortar method due to a multiplication of two averaged quantities an inner assembly loop evolves in this case [30] leading to an additional computational effort. Hence the tangential contact weak form is written in a Hellinger-Reissner description introducing additional Lagrange multipliers which increases the CPU time considerably to a lesser extend

$$G_{l_T}^c = \int_{\partial B_c} \delta\lambda_{T\alpha} \frac{1}{c_T} [\lambda_{T\alpha} - t_{T\alpha}] \, da = 0. \quad (10)$$

The equation states that the Lagrange multiplier has to be equal to the tangential stress components  $t_{T\alpha}$ . The solution algorithm for  $t_{T\alpha}$  will be presented in section 4 and 5.

For the discretization of the contact weak form the Mortar method is applied which can be viewed as the most robust solution technique for contact applications at the moment. This method was originally developed to couple finite with spectral elements [32],[33] and was extended to contact cases for instance in [19],[34],[22]. In contrast to the node-to-segment formulation [16],[26] all quantities are discretized and integrated numerically like in finite elements for the continuum. The key approach of the Mortar method will be explained schematically for the normal contact constraint and will be applied later on to other parts of the contact weak form. In computational contact mechanics the slave side is viewed as the contact surface. Normally, the discretization procedure in finite elements would be to sum up over all elements  $n_s$  of this contact surface

$$\int_{\partial B_c} \delta\lambda_N g_N \, da = \sum_{e=1}^{n_s} \sum_{g=1}^{n_{gp}^e} \sum_{A=1}^{N_s^e} N_A \delta\lambda_{NA} \sum_{B=1}^{N_s^e} N_B g_{NB} \det \mathbf{j}_g^e W_g. \quad (11)$$

The integration is done on a reference element using a specific number of integration points  $n_{gp}^e$  within that element and  $N_s^e$  indicates the number of nodes of the surface element. In the Mortar method the discretization process is reformulated into a summation over all slave nodes  $N_s$  instead of a summation over all slave elements

$$\int_{\partial B_c} \delta \lambda_N g_N \, da = \sum_{A=1}^{N_s} \delta \lambda_{NA} \sum_{e=1}^{n_s^A} \sum_{g=1}^{n_{gp}^e} N_A \sum_{B=1}^{N_s^e} N_B g_{NB} \det \mathbf{j}_g^e W_g. \quad (12)$$

Now at each node  $A$  the contributions of all adjacent elements  $n_s^A$  of that node has to be added up. The term on the right side of the virtual normal Lagrange multiplier can be viewed as a nodal average of the normal gap. This averaging procedure is similar to the computation of the nodal stress in the post-processing of a finite element program. Finally the discretized weak form of the normal constraint leads in the Mortar framework to

$$\int_{\partial B_c} \delta \lambda_N g_N \, da = \sum_{A=1}^{N_s} \delta \lambda_{NA} \bar{g}_{NA}, \quad \bar{g}_{NA} = \sum_{e=1}^{n_s^A} \sum_{g=1}^{n_{gp}^e} N_A \sum_{B=1}^{N_s^e} N_B g_{NB} \det \mathbf{j}_g^e W_g \quad (13)$$

where the bar over the quantity indicates an averaged value. Subsuming the summation over adjacent elements and integration points to a summation over the whole integration points in all adjacent elements  $n_{gp}$  the normal penetration and its variation can be written in more detail as

$$\begin{aligned} \bar{g}_{NA} &= \sum_{g=1}^{n_{gp}} N_A (\boldsymbol{\xi}_{g n+1}^1) (\mathbf{x}_{n+1}^2 (\boldsymbol{\xi}_{g n+1}^2) - \mathbf{x}_{n+1}^1 (\boldsymbol{\xi}_{g n+1}^1)) \cdot \mathbf{n}_{n+1}^1 (\boldsymbol{\xi}_{g n+1}^1) \det \mathbf{j}_{n+1} W_g \\ \delta \bar{g}_{NA} &= \sum_{g=1}^{n_{gp}} N_A (\boldsymbol{\xi}_{g n+1}^1) (\boldsymbol{\eta}_{n+1}^2 (\boldsymbol{\eta}_{g n+1}^2) - \boldsymbol{\eta}_{n+1}^1 (\boldsymbol{\xi}_{g n+1}^1)) \cdot \mathbf{n}_{n+1}^1 (\boldsymbol{\xi}_{g n+1}^1) \det \mathbf{j}_{n+1} W_g. \end{aligned} \quad (14)$$

The position of each quantity at the integration point, like the position vectors at each surface, the normal base vector or the normal Lagrange multiplier, can be obtained by using standard surface shape functions

$$\begin{aligned} \mathbf{x}_{n+1}^1 (\boldsymbol{\xi}_{g n+1}^1) &= \sum_{B=1}^{N_s^e} N_B (\boldsymbol{\xi}_{g n+1}^1) \mathbf{x}_{B n+1}^1, & \mathbf{x}_{n+1}^2 (\boldsymbol{\xi}_{g n+1}^2) &= \sum_{C=1}^{N_m^e} N_C (\boldsymbol{\xi}_{g n+1}^2) \mathbf{x}_{C n+1}^2 \\ \mathbf{n}_{n+1}^1 (\boldsymbol{\xi}_{g n+1}^1) &= \sum_{B=1}^{N_s^e} N_B (\boldsymbol{\xi}_{g n+1}^1) \mathbf{n}_{B n+1}^1, & \lambda_{N n+1} (\boldsymbol{\xi}_{g n+1}^1) &= \sum_{B=1}^{N_s^e} N_B (\boldsymbol{\xi}_{g n+1}^1) \lambda_{NB n+1}. \end{aligned} \quad (15)$$

For the averaged quantities the index  $n+1$  is neglected to ease the notation, since all averaged quantities are written with respect to the actual time step. If values at the previous time step occur, they will be denoted further with the index  $n$ . Additionally,  $\boldsymbol{\xi}^1$  and  $\boldsymbol{\xi}^2$  corresponds to the coordinates of the integration points at the slave and at the master surface, respectively. The averaging process for the normal penetration is similar to [35], but different to the formulations in other Mortar formulations given for instance in [34],[22] where only the gap is averaged and the penetration is computed by  $\bar{g}_{NA} = \bar{\mathbf{g}}_A \cdot \mathbf{n}_A$ . For the time integration of the evolution equation (5) the implicit backward Euler scheme is used. In the discretization process of the Mortar method the components of the increment of the tangential gap

have to be averaged  $\Delta_t \bar{g}_{T\alpha A} = \bar{g}_{T\alpha A} - \bar{g}_{T\alpha A}^o$ . This process follows accordingly to (14)

$$\begin{aligned}\bar{g}_{T\alpha A} &= \sum_{g=1}^{n_{gp}} N_A(\boldsymbol{\xi}_{g n+1}^1) (\mathbf{x}_{n+1}^2(\boldsymbol{\xi}_{g n+1}^2) - \mathbf{x}_{n+1}^1(\boldsymbol{\xi}_{g n+1}^1)) \cdot \mathbf{t}_{\alpha n+1}^1(\boldsymbol{\xi}_{g n+1}^1) \det \mathbf{j}_{n+1} W_g \\ \delta \bar{g}_{T\alpha A} &= \sum_{g=1}^{n_{gp}} N_A(\boldsymbol{\xi}_{g n+1}^1) (\boldsymbol{\eta}_{n+1}^2(\boldsymbol{\xi}_{g n+1}^2) - \boldsymbol{\eta}_{n+1}^1(\boldsymbol{\xi}_{g n+1}^1)) \cdot \mathbf{t}_{\alpha n+1}^1(\boldsymbol{\xi}_{g n+1}^1) \det \mathbf{j}_{n+1} W_g \\ \bar{g}_{T\alpha A}^o &= \sum_{g=1}^{n_{gp}} N_A(\boldsymbol{\xi}_{g n}^1) (\mathbf{x}_{n+1}^2(\boldsymbol{\xi}_{g n}^2) - \mathbf{x}_{n+1}^1(\boldsymbol{\xi}_{g n}^1)) \cdot \mathbf{t}_{\alpha n+1}^1(\boldsymbol{\xi}_{g n}^1) \det \mathbf{j}_n W_g.\end{aligned}\quad (16)$$

Within the averaged old tangential gap  $\bar{g}_{T\alpha A}^o$  only the integration points are specified at the previous time step to guarantee an objective measure for the tangential movement, see also [36] for more details. In the case of the weak form of the tangential contact constraints (10) and in the case of no contact (9) the Lagrange multipliers have to be averaged as well

$$\begin{aligned}\bar{\lambda}_{NA} &= \sum_{g=1}^{n_{gp}} N_A(\boldsymbol{\xi}_{g n+1}) \lambda_{N n+1}(\boldsymbol{\xi}_{g n+1}^1) \det \mathbf{j}_{n+1} W_g \\ \bar{\lambda}_{T\alpha A} &= \sum_{g=1}^{n_{gp}} N_A(\boldsymbol{\xi}_{g n+1}) \lambda_{T\alpha n+1}(\boldsymbol{\xi}_{g n+1}^1) \det \mathbf{j}_{n+1} W_g.\end{aligned}\quad (17)$$

To have uniquely defined base vectors at each slave node  $A$ , the nodal base vector contributions of each adjacent element of that node  $\bar{\boldsymbol{\xi}}_A$  are added up

$$\mathbf{a}_{\alpha A n+1}^1 = \sum_{e=1}^{n_s^A} \sum_{I=1}^{N_s^e} N_{I,\alpha}(\bar{\boldsymbol{\xi}}_A) \mathbf{x}_{I n+1}^1 \quad (18)$$

which is shown schematically for the 2D case in figure 3. Using normalized base vectors, like in [29],[31],

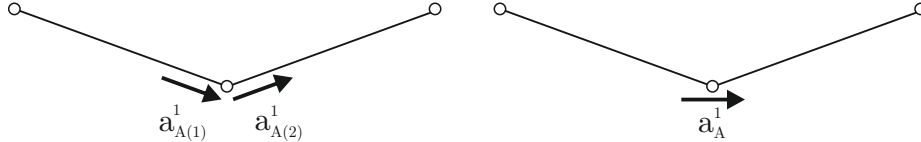


Figure 3: Averaged base vector schematically for the 2D case

the tangential base vectors  $\mathbf{t}_{\alpha A}^1$  and the normal base vector  $\mathbf{n}_A^1$  at each contact node are given by

$$\mathbf{t}_{\alpha A n+1}^1 = \frac{\mathbf{a}_{\alpha A n+1}^1}{\|\mathbf{a}_{\alpha A n+1}^1\|}, \quad \mathbf{n}_A^1 = \frac{\mathbf{a}_{1 A n+1}^1 \times \mathbf{a}_{2 A n+1}^1}{\|\mathbf{a}_{1 A n+1}^1 \times \mathbf{a}_{2 A n+1}^1\|}. \quad (19)$$

Following the outcome in [37], to pass the patch test an exact integration of the integrals over the slave surface in (7),(9),(10) or respectively within the averaged kinematical quantities (14),(16),(17) should be preferred. To ensure this feature almost exactly Puso [34] developed a segment-to-segment algorithm introducing an even reference plan akin to the standard finite element method. First, each slave element is transformed into an even reference plane. Afterward all nodes of each master element are projected onto this plane and a clipping algorithm, like [38] is used to compute the intersection points (figure 4).

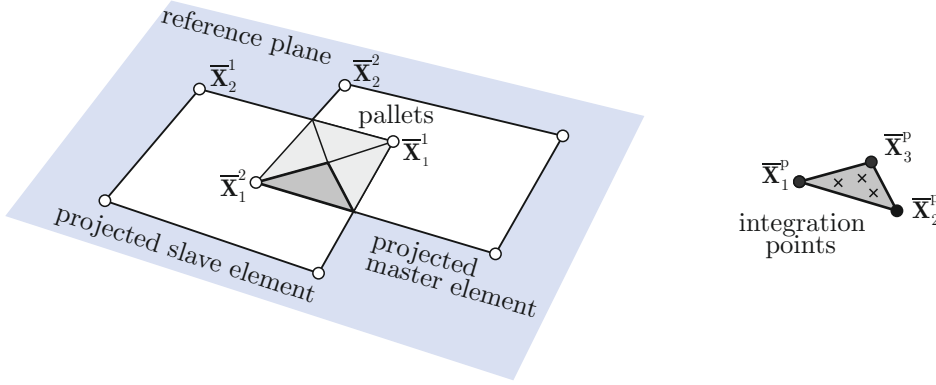


Figure 4: Clipping of one slave and one master element (left) and integration points within one pallet (right)

The resulting overlap between one slave and one master element is called a segment and it is further subdivided into triangular pallets (figure 4) locating the integration points on the reference plane. Finally, these points are back projected onto each surface locating the integration points within the slave and the corresponding master element. The Jacobian can then be defined for each pallet as the area of the triangle

$$\det \mathbf{j}_{n+1} = \frac{1}{2} \| (\bar{\mathbf{x}}_{2n+1}^p - \bar{\mathbf{x}}_{1n+1}^p) \times (\bar{\mathbf{x}}_{3n+1}^p - \bar{\mathbf{x}}_{1n+1}^p) \| \quad (20)$$

and  $W_g$  in (14),(16) and (17) corresponds to the weighting of that triangle. Now the summation over all integration points in (14),(16) and (17) can be specified in detail as the summation over all elements adjacent to that node  $n_s^A$ , over all segments within each element  $n_{seg}$ , over all pallets  $n_{pa}$  and over all integration points of the triangular pallet  $n_{gp}^{pa}$

$$\sum_{g=1}^{n_{gp}} = \sum_{a=1}^{n_s^A} \sum_{s=1}^{n_{seg}} \sum_{p=1}^{n_{pa}} \sum_{t=1}^{n_{gp}^{pa}}. \quad (21)$$

Finally, using the averaged kinematical quantities (14) and (16) the weak form of the contact contributions in (7),(9) and (10) can be reformulated into a summation over all slave nodes. The weak form of virtual contact work

$$G_u^c = \sum_{A=1}^{n_s} \left[ \delta \bar{g}_{NA} \lambda_{NA n+1} + \delta \bar{g}_{T\alpha A} \lambda_{T\alpha A n+1} \right] \quad (22)$$

and the weak form of the normal and of the tangential contact constraint for an active node  $\bar{\lambda}_{NA} + c_N \bar{g}_{NA} \leq 0$  change to

$$G_l^c = \sum_{A=1}^{n_s} \left[ \delta \lambda_{NA n+1} \bar{g}_{NA} + \delta \lambda_{T\alpha A n+1} \frac{1}{c_T} (\bar{\lambda}_{T\alpha A} - \bar{t}_{T\alpha A}) \right] = 0. \quad (23)$$

In the case the slave node is not active  $\bar{\lambda}_{NA} + c_N \bar{g}_{NA} > 0$  an additional constraint is introduced ensuring that the averaged normal and tangential Lagrange multipliers are equal to zero

$$G_l^c = \sum_{A=1}^{n_s} \left[ \delta \lambda_{NA n+1} \frac{1}{c_N} \bar{\lambda}_{NA} + \delta \lambda_{T\alpha A n+1} \frac{1}{c_T} \bar{\lambda}_{T\alpha A} \right] = 0. \quad (24)$$

### 3 Soil model

The application of the developed projection schemes is the improvement of the simulation of soil-structure interactions. Therefore a proper soil description is needed. Among many different models Ehlers [23],[24] developed a generic elasto-plastic formulation able to take into account the pressure dependency of the friction angle and the dependency of the admissible elastic domain on the Lode angle. The porosity of the soil is considered by the factor  $c^v$  given within the linear elastic stress strain relation

$$\boldsymbol{\sigma} = \lambda \operatorname{tr} \boldsymbol{\varepsilon}^e c^v + 2\mu \boldsymbol{\varepsilon}^e \quad (25)$$

where the factor  $c^v$  [24] describes the influence of the solid volume ratio limited by its initial value  $n_0^s$  and its upper bound  $n_{max}^s$

$$c^v = \frac{\operatorname{tr} \boldsymbol{\varepsilon}^c}{(\operatorname{tr} \boldsymbol{\varepsilon}^c - \operatorname{tr} \boldsymbol{\varepsilon}^e)}, \quad \operatorname{tr} \boldsymbol{\varepsilon}^c = \frac{n_p^s}{n_{max}^s} - 1 = \frac{n_0^s}{n_{max}^s (1 + \operatorname{tr} \boldsymbol{\varepsilon}^p)} - 1. \quad (26)$$

The yield criterion bounding the admissible elastic domain is formulated in terms of the first invariant of the stress tensor  $I_\sigma$  as well as of the second  $II_s$  and of the third invariant  $III_s$  of the deviatoric stress  $\mathbf{s}$

$$f(\boldsymbol{\sigma}) = \sqrt{\left(1 + \gamma III_s II_s^{-\frac{3}{2}}\right)^m II_s + \frac{1}{2} \alpha I_\sigma^2 + \delta^2 I_\sigma^4 + \beta I_\sigma + \epsilon I_\sigma^2 - \kappa} = 0. \quad (27)$$

Seven parameters ( $\alpha, \beta, \gamma, \delta, \epsilon, \kappa, m$ ) have to be determined by proper material tests [23] where the friction angle  $\varphi$  and the cohesion  $c$  are linked to the model via  $\kappa = c \cos \varphi$  and  $\beta = \frac{1}{3} \sin \varphi$ . To ensure a correct dilatancy or contractancy behavior of the soil in this model a non associated description is used leading to the potential  $g(\boldsymbol{\sigma})$

$$g(\boldsymbol{\sigma}) = \sqrt{\Psi_1 II_s + \frac{1}{2} \alpha I_\sigma^2 + \delta^2 I_\sigma^4 + \Psi_2 \beta I_\sigma + \epsilon I_\sigma^2} \quad (28)$$

where two additional parameters ( $\Psi_1, \Psi_2$ ) are introduced into the model. The evolution equation of the plastic strain is given by the derivative of the potential with respect to the stress tensor multiplied with the plastic rate  $\dot{\lambda}$

$$\dot{\boldsymbol{\varepsilon}}^p = \dot{\lambda} \frac{\partial g(\boldsymbol{\sigma})}{\partial \boldsymbol{\sigma}} = \frac{1}{2g_{rt}} [\Psi_1 \mathbf{s} + (\alpha I_\sigma + 4\delta^2 I_\sigma^3) \mathbf{1}] + (\Psi_2 \beta + 2\epsilon I_\sigma) \mathbf{1} \quad (29)$$

$$g_{rt} = \sqrt{\Psi_1 II_s + \frac{1}{2} \alpha I_\sigma^2 + \delta^2 I_\sigma^4}.$$

A measure able to determine the dilatant or contractant behavior of a material point is formulated by the tangent of the dilatancy angle  $\nu^p$  which corresponds to the quotient of the volumetric plastic strain to the norm of its deviatoric part

$$\tan \nu^p = \frac{\dot{\boldsymbol{\varepsilon}}^p \cdot \mathbf{1}}{3 \|\dot{\boldsymbol{\varepsilon}}^p\|}. \quad (30)$$

The tensor  $\dot{\boldsymbol{\varepsilon}}^p = \dot{\boldsymbol{\varepsilon}}^p - 1/3(\dot{\boldsymbol{\varepsilon}}^p \cdot \mathbf{1}) \mathbf{1}$  used in (30) indicates the deviatoric part of the rate of the plastic strain. For the Ehlers soil model the tangent of the dilatancy angle can be written explicitly as

$$\tan \nu^p = \frac{1}{\Psi_1 \sqrt{2II_s}} \left[ \alpha I_\sigma + 4\delta^2 I_\sigma^3 + 2 \sqrt{\Psi_1 II_s + \frac{1}{2} \alpha I_\sigma^2 + \delta^2 I_\sigma^4} (\Psi_2 \beta + 2\epsilon I_\sigma) \right]. \quad (31)$$

Since the soil has a highly nonlinear plastic behavior, an additional equation is needed to take into account hardening and softening effects. In the Ehlers soil model an evolution equation of four parameters  $\mathbf{h} = [\beta, \gamma, \delta, \epsilon]^T$  describes these effects

$$\dot{\mathbf{h}} = \dot{\lambda} (\mathbf{h}_{max} - \mathbf{h}) \left[ \mathbf{C}_h^v \tan \nu^p + \mathbf{C}_h^d \right] \|\dot{\epsilon}^p\| = 0 \quad (32)$$

where  $\mathbf{h}_{max}$  corresponds to the maximum values of the parameters. The actual stress is computed from the constitutive equations (25) - (32) and the numerical solution is based on the implicit return mapping algorithm [39]. A detailed implementation can be found in [20],[40]. Unfortunately, in the case of a plastic response, due to the conical structure of the yield surface in stress space, the back-projection within the return mapping algorithm onto the surface can fail, especially close the apex. This is especially true when the trial stress and the trial hardening parameters are far away from the projection point (figure 5). Hence a projection to different solutions can occur which leads to a non convergence of the algorithm.

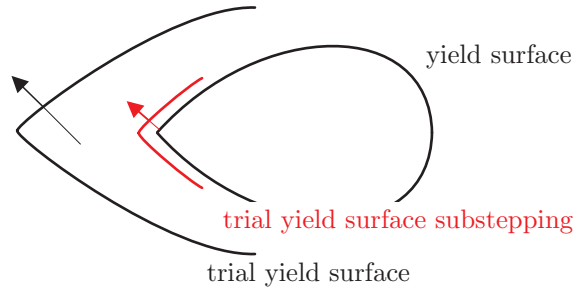


Figure 5: Difference between standard and substepping back-projection schemes

A possibility to improve the closest point projection algorithm is the use of a substepping scheme [41] which is based on line search techniques. A numerical implementation within the implicit return mapping algorithm can be found in [42]. Within the substepping algorithm at each integration point the trial elastic strain is subdivided into a number of increments (*steps*) which ensures that the trial value remains always closely to the projection point (figure 5). Within an additional loop  $k = 1, steps$  the actual stress and the material tangent has to be solved at each step  $k$  together with the culminated strain and its updated plastic part

$$q^{(k)} = \sum_{i=1}^k s^{(i)}, \quad \epsilon_{n+1}^{(k)} = q^{(k)} \epsilon_{n+1}, \quad \epsilon_{n+1}^{p(k)} = s^{(k)} \epsilon_n^p + \gamma_{n+1}^{(k)} \left. \frac{\partial \mathbf{g}}{\partial \boldsymbol{\sigma}} \right|_{n+1}^{(k)} + \epsilon_{n+1}^{p(k-1)}. \quad (33)$$

Another challenge is the oscillation between the elastic and the plastic state of the material point that leads also to a non converging of the overall solution algorithm. Remedies to overcome such cases are viscoplastic regularization. One formulation presented in [43] and numerical implemented in [44] is applied to the Ehlers soil model

$$\boldsymbol{\sigma}_{n+1} = \boldsymbol{\sigma}_{n+1}^* + \frac{\eta/\Delta t}{1 + \eta/\Delta t} (\boldsymbol{\sigma}_{n+1}^{tr} - \boldsymbol{\sigma}_{n+1}^*). \quad (34)$$

Within this formulation the elastic domain is extended temporarily between the trial elastic  $\boldsymbol{\sigma}_{n+1}^{tr}$  and the back-projected stress  $\boldsymbol{\sigma}_{n+1}^*$  by means of a damping parameter  $\eta$ .

## 4 Projection based on the transition of plasticity to friction

The formulations and solution techniques related to the elasto-plastic theory and related to the frictional contact behavior have a lot in common. The yield criterion bounding the elastic domain is similar to the slip rule limiting the stick case. Furthermore the evolution equation for the plastic strain corresponds to the evolution equation for the tangential movement. Despite all similarities, unfortunately, a direct transition from plasticity to friction is not possible. The stress dependency within the yield criterion is often expressed by means of three invariants whereas in the slip rule the norm of the tangential stress and the normal pressure only influence the tangential behavior. Using a return mapping algorithm for the solution of the frictional contact behavior a back-projection in the direction of the desired tangential stress is only allowed which is equivalent to a dilatancy angle of zero degree. A positive dilatancy angle would lead to a release of the contact, although the pressure between the bodies is non zero and a negative dilatancy angle would lead to a normal penetration which is not allowed. Therefore, to incorporate the dilatancy effects at the contact layer an additional contact stress component is introduced. The projection scheme is explained here exemplary for the contact formulation given in section 2, but it can be applied to all other types of contact discretization techniques.

### 4.1 Projection scheme

One of the oldest model describing especially granular materials is the Mohr-Coulomb yield criterion which structure is similar to other plasticity formulations like Drucker-Prager, Tresca or von Mises. The Mohr-Coulomb yield criterion  $f^m$  suitable especially for the description of soil behavior is the 3-dimensional extension of the Coulomb slip rule  $f^c$ , see [13] for a derivation

$$f^c = \|\bar{\mathbf{t}}_{TA n+1}\| + \bar{\lambda}_{NA n+1} \tan \varphi = 0$$

$$f^m = \frac{\sqrt{\Pi_{\mathbf{s} n+1} \cos \Theta_{n+1}}}{\cos \varphi} + \left[ \frac{1}{3} \mathbf{I}_{\sigma n+1} - \sqrt{\frac{\Pi_{\mathbf{s}}}{3}} \sin(\Theta)_{n+1} \right] \tan \varphi = 0. \quad (35)$$

In this formulation the three continuum quantities  $\mathbf{I}_{\sigma n+1}$ ,  $\sqrt{\Pi_{\mathbf{s} n+1}}$ ,  $\Theta_{n+1}$  can not be related directly to the two contact invariants  $\bar{\lambda}_{NA n+1}$ ,  $\|\bar{\mathbf{t}}_{TA n+1}\|$ . However, since the tangential contact motion is equivalent to shearing with a load on top, the Lode angle

$$\Theta_{n+1} = -\frac{1}{3} \arcsin \left( \frac{\sqrt{27} \Pi_{\mathbf{s} n+1}}{2 \Pi_{\mathbf{s} n+1}^{\frac{3}{2}}} \right) \quad (36)$$

can be assumed to be zero  $\Theta_{n+1} = 0^\circ$ . Now the invariants of the frictional formulation and of the plasticity model can be related directly and so called contact stress invariants can be defined

$$\begin{aligned} \Pi_{\mathbf{s}A n+1} &:= \|\bar{\mathbf{t}}_{TA n+1}\|^2 \cos^2 \varphi \\ \mathbf{I}_{\sigma A n+1} &:= 3 \bar{\lambda}_{NA n+1}, \quad \Theta_{A n+1} := 0^\circ. \end{aligned} \quad (37)$$

Accordingly, the tangential contact stress depends on the second invariant of the deviatoric stress and on the friction angle. The normal stress is only related to the first invariant of the stress itself. A demonstrative explanation is illustrated in figure 6 showing that the slip criterion results from the yield

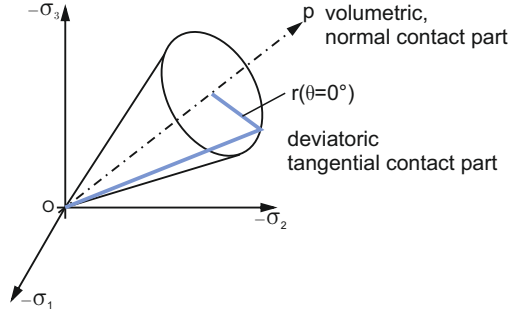


Figure 6: Cut through the yield surface at a Lode angle of  $0^\circ$

surface by a cut through the surface at a Lode angle of  $0^\circ$  corrected by the slip angle. A split of the back-projection of the trial stress onto the yield surface into a volumetric and a deviatoric part leads to the corresponding formulations for the two invariants

$$\begin{aligned} I_{\boldsymbol{\sigma}_{n+1}} &= I_{\boldsymbol{\sigma}_{n+1}}^{tr} - 9 K \gamma_{n+1} \frac{\partial g(I_{\boldsymbol{\sigma}_{n+1}}, \Pi_{\mathbf{s}_{n+1}})}{\partial I_{\boldsymbol{\sigma}_{n+1}}} \\ \sqrt{\Pi_{\mathbf{s}_{n+1}}} &= \sqrt{\Pi_{\mathbf{s}_{n+1}}^{tr}} - 2 \mu \gamma_{n+1} \frac{\partial g_{n+1}}{\partial \Pi_{\mathbf{s}_{n+1}}} \sqrt{\Pi_{\mathbf{s}_{n+1}}}. \end{aligned} \quad (38)$$

Due to the assumption of a zero Lode angle the plastic potential depends only on  $I_{\boldsymbol{\sigma}_{n+1}}, \Pi_{\mathbf{s}_{n+1}}$ . Together with the link between the continuum stress invariants and the contact quantities (37) the algorithms computing the normal and tangential contact stress can be stated. Unfortunately, the back-projection of the normal contact stress is physically not feasible. A dilatant behavior leads to a release of the contact and contractancy to a penetration of one body into the other which is not allowed. Looking at the graphical illustration in figure 7 the back-projected normal stress component can be interpreted as

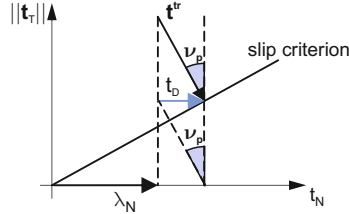


Figure 7: Graphical illustration of the two constituents of the normal contact stress

the sum of the normal pressure together with an additional stress contribution  $t_{DA n+1}$ . This additional stress corresponds exactly to the back-projected norm of the tangential stress multiplied with the tangent of the dilatancy angle

$$\bar{t}_{DA n+1} = -\tan \nu_{A n+1}^p \|\bar{\mathbf{t}}_{TA n+1}\|. \quad (39)$$

The minus sign has to be added, since normal stress contributions and not the pressure is considered. Instead of the back-projection (38) the actual first invariant is computed alternatively as

$$I_{\boldsymbol{\sigma}_{n+1}} = 3 \bar{\lambda}_{NA n+1} - 3 \tan \nu_{A n+1}^p \|\bar{\mathbf{t}}_{TA n+1}\| \quad (40)$$

The numerical algorithm to compute the tangential contact stress follows directly from (38) using relation (37) and the fact that the trial and the actual tangential stress is pointing towards the same direction, see also [16]

$$\bar{\mathbf{t}}_{TA n+1} = \bar{\mathbf{t}}_{TA n+1}^{tr} + 2\mu\gamma_{n+1} \frac{\partial g(\mathbf{I}_{\sigma n+1}, \mathbf{\Pi}_{\mathbf{s} n+1})}{\partial \mathbf{\Pi}_{\mathbf{s} n+1}} \bar{\mathbf{t}}_{TA n+1} \quad (41)$$

Within (41) to ease the computation the trial friction angle is assumed to be equal to the actual and to the previous slip angle

$$\varphi_{A n+1}^{tr} = \varphi_{A n+1} = \varphi_{A n} = \arctan\left(\frac{\|\bar{\mathbf{t}}_{TA n}\|}{|\bar{\mathbf{t}}_{NA n}|}\right). \quad (42)$$

This assumption can be made, since in the simulation of the soil behavior the time intervals have normally to be small and the change of the friction angle during one step is marginal. The tangential contact stress of the trial state is computed analogous to standard contact formulations, see [16]

$$\bar{\mathbf{t}}_{TA n+1}^{tr} = -\frac{2\mu}{\delta_T a_{A n+1}} [\bar{\mathbf{g}}_{TA n+1} - \bar{\mathbf{g}}_{TA n+1}^o] + \bar{\mathbf{t}}_{TA n}^e. \quad (43)$$

where  $\bar{\mathbf{g}}_{TA n+1} - \bar{\mathbf{g}}_{TA n+1}^o$  is the increment of the tangential movement, see also equation (16). The penalty parameter for the tangential part is linked here to the shear modulus by a parameter  $\delta_T$

$$c_T = \frac{2\mu}{\delta_T}. \quad (44)$$

To ensure stress values using the Mortar method the tangential gap has to be divided by its area

$$a_{A n+1} = \sum_{g=1}^{n_{gp}} \det \mathbf{j}_{n+1} W_g. \quad (45)$$

## 4.2 Projection of Ehlers soil model

Due to the assumption of a Lode angle of zero degree the yield criterion of the soil model of Ehlers (27) changes to

$$f_{n+1} = \sqrt{\mathbf{\Pi}_{\mathbf{s} n+1} + \frac{1}{2}\alpha(\mathbf{I}_{\sigma n+1})^2 + \delta_{A n+1}^2(\mathbf{I}_{\sigma n+1})^4 + \beta_{A n+1}\mathbf{I}_{\sigma n+1} + \epsilon_{A n+1}(\mathbf{I}_{\sigma n+1})^2}. \quad (46)$$

The derivatives of the potential (28) with respect to the deviatoric stress remains equal to the continuum case

$$\frac{\partial g(\mathbf{I}_{\sigma n+1}, \mathbf{\Pi}_{\mathbf{s} n+1})}{\partial \mathbf{\Pi}_{\mathbf{s} n+1}} = \frac{\Psi_1}{2\sqrt{\Psi_1\mathbf{\Pi}_{\mathbf{s} n+1} + \frac{1}{2}\alpha\mathbf{I}_{\sigma n+1}^2 + \delta^2\mathbf{I}_{\sigma n+1}^4}}. \quad (47)$$

and the evolution equation of the hardening parameters (32) remains also unchanged

$$\mathbf{h}_{A n+1} = \mathbf{h}_{A n} + \gamma_{n+1}(\mathbf{h}_{max} - \mathbf{h}_{A n+1}) \left[ \mathbf{C}_h^v \tan \nu_{A n+1}^p + \mathbf{C}_h^d \right] \frac{\partial g_{n+1}}{\partial \mathbf{\Pi}_{\mathbf{s} n+1}} \sqrt{2\mathbf{\Pi}_{\mathbf{s} n+1}} \quad (48)$$

as well as the tangent of the dilatancy angle given in (31)

$$\tan \nu_{A n+1}^p = \frac{1}{\Psi_1 \sqrt{2\mathbf{\Pi}_{\mathbf{s} n+1}}} \left[ \alpha \mathbf{I}_{\sigma n+1} + 4\delta_{A n+1}^2 \mathbf{I}_{\sigma n+1}^3 + 2\sqrt{\Psi_1 \mathbf{\Pi}_{\mathbf{s} n+1} + \frac{1}{2}\alpha \mathbf{I}_{\sigma n+1}^2 + \delta_{A n+1}^2 \mathbf{I}_{\sigma n+1}^4} (\Psi_2 \beta_{A n+1} + 2\epsilon \mathbf{I}_{\sigma n+1}) \right]. \quad (49)$$

The starting value for the slip angle is assumed as

$$\varphi_{A0} = \arcsin(3\beta_{A0}) \quad (50)$$

The computation of the stick or slip case follows analogous to the standard frictional computation, see for instance [16]

$$f(\bar{\mathbf{t}}_{TA_{n+1}}, \bar{\lambda}_{NA_{n+1}}, \mathbf{h}_{A_{n+1}}^{tr}) < \delta \rightarrow \text{stick}, \quad f(\bar{\mathbf{t}}_{TA_{n+1}}, \bar{\lambda}_{NA_{n+1}}, \mathbf{h}_{A_{n+1}}^{tr}) \geq \delta \rightarrow \text{slip} \quad (51)$$

where  $\delta$  is a parameter close to zero due to numerical reasons. In the stick case the actual stress components and the hardening parameters correspond exactly to the trial ones

$$\bar{\mathbf{t}}_{TA_{n+1}} = \bar{\mathbf{t}}_{TA_{n+1}}^{tr}, \quad \mathbf{h}_A = \mathbf{h}_A^{tr}. \quad (52)$$

In the slip case the residual equations for the tangential stress component, the evolution of the hardening parameters, the tangent of the dilatancy angle and the slip criterion

$$\begin{aligned} \mathbf{R}_T &= \frac{\delta_T}{2\mu} (\bar{\mathbf{t}}_{T_{n+1}} - \bar{\mathbf{t}}_{T_{n+1}}^{tr}) + \gamma_{n+1} \frac{\partial g(\mathbf{I}_{\sigma_{n+1}}, \mathbf{II}_{\mathbf{s}_{n+1}})}{\partial \mathbf{II}_{\mathbf{s}_{n+1}}} \bar{\mathbf{t}}_{TA_{n+1}} = 0 \\ \mathbf{R}_H &= \mathbf{h}_{A_{n+1}} - \mathbf{h}_{A_n} - \gamma_{n+1} (\mathbf{h}_{max} - \mathbf{h}_{n+1}) \left[ \mathbf{C}_h^v \tan \nu_{A_n}^p + \mathbf{C}_h^d \right] \frac{\partial g_{n+1}}{\partial \mathbf{II}_{\mathbf{s}_{n+1}}} \sqrt{2 \mathbf{II}_{\mathbf{s}_{n+1}}} = 0 \\ \mathbf{R}_\nu &= \tan \nu_{A_{n+1}}^p - \frac{1}{\Psi_1 \sqrt{2 \mathbf{II}_{\mathbf{s}_{n+1}}}} \left[ \alpha \mathbf{I}_{\sigma_{n+1}} + 4 \delta_{A_{n+1}}^2 \mathbf{I}_{\sigma_{n+1}}^3 \right. \\ &\quad \left. + 2 \sqrt{\Psi_1 \mathbf{II}_{\mathbf{s}_{n+1}} + \frac{1}{2} \alpha \mathbf{I}_{\sigma_{n+1}}^2 + \delta_{A_{n+1}}^2 \mathbf{I}_{\sigma_{n+1}}^4} (\Psi_2 \beta_{A_{n+1}} + 2 \epsilon \mathbf{I}_{\sigma_{n+1}}) \right] = 0 \\ \mathbf{R}_\gamma &= f_{n+1} = 0. \end{aligned} \quad (53)$$

have to be equal to zero. Since the equations are nonlinear with respect to the contact invariants, the Newton iteration is applied to determine the tangential stress, the hardening parameters and the tangent of the dilatancy angle that fulfill the slip rule. The linearization of the tangential stress follows then directly from the tangent together with the modified residual vector which is analogous to the case of plasticity. A detailed explanation for that case can be found for instance in [28].

### 4.3 Numerical direct shear test

In soil mechanics two different tests are often conducted to determine the shear behavior of the material under investigation. The triaxial shear test is a typical 3-dimensional test procedure whereas the direct shear test characterizes the soil behavior over a relative movement of the contacting specimen. However both tests have the same outcome. In the following numerical example the soil-structure interaction of a block of steel ( $E = 210 \cdot 10^3 \text{ MN/m}^2$ ,  $\nu = 0.2$ ) with a soil specimen of dense GEBA fine sand is investigated where the surface of the steel block is assumed to be rough. Due to the roughness the sand is dominating the shear behavior and the direct shear test deliver the same response as the 3-dimensional triaxial test which can be seen in experimental investigations [5]. For the description of the material behavior of the GEBA fine sand the Ehlers soil model of section 3 is used. The associated material

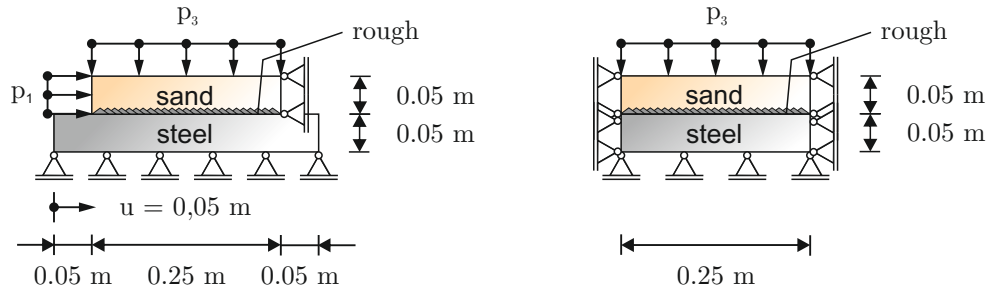


Figure 8: Side view and front view of the direct shear test with a rough surface

parameters are given in table 1. On top of the test apparatus a variable surface pressure is applied. Furthermore, the soil specimen and the block of steel are fixed in the horizontal direction. In order to avoid tension within the soil specimen on the side where the tangential displacement is applied a pressure of  $p_1 = 0.5 \text{ kN/m}^2$  ensures positive stress values within the soil (figure 8). For each projection concept a series of different vertical pressure loads is investigated. In order to compare the reproducibility of the continuum behavior at the contact surface all the results are compared with the same direct shear test where now one layer of continuum elements is located in between of the two plates as can be seen in figure 9.

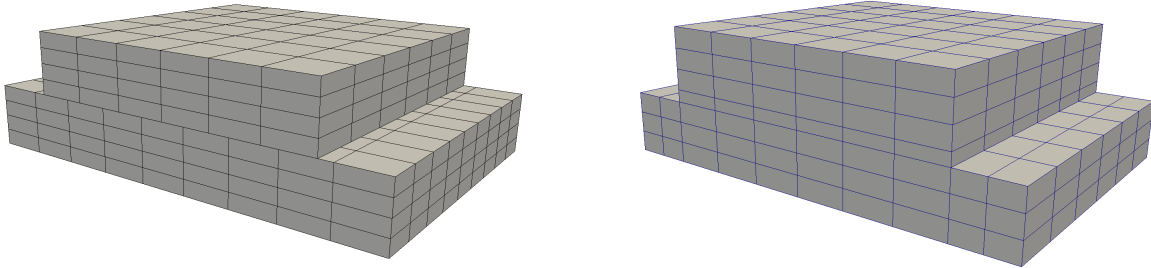


Figure 9: Finite element mesh of the contact case (left) and of the continuum case with one layer of elements between the two bodies (right)

Comparing the force distribution along the sliding distance a different behavior is obvious (figure 10). In the interface element during the phase when the pressure is imposed a plastic response behavior can be observed already. In the contact model only stick occurs in the first loading situation. Hence the evolution of the hardening behavior starts not before sliding and then in a more moderate fashion. The Lode angle is not exactly zero in the case of dilatancy or contractancy and leads to a small under-prediction of the stress in normal direction although dilatancy was included in the formulation. Additionally, it can be seen from figure 10 that the change of the height of the interface element has not a strong influence on the final result. Only the peak behavior is slightly different at the onset of sliding. Nevertheless the distribution of the final friction angle as well as of the final tangential force over the normal pressure are qualitatively in a good accordance as can be seen in figure 11. Beside the possibility of arbitrary large relative movements between the soil and the structure another advantage of the projected contact formulation

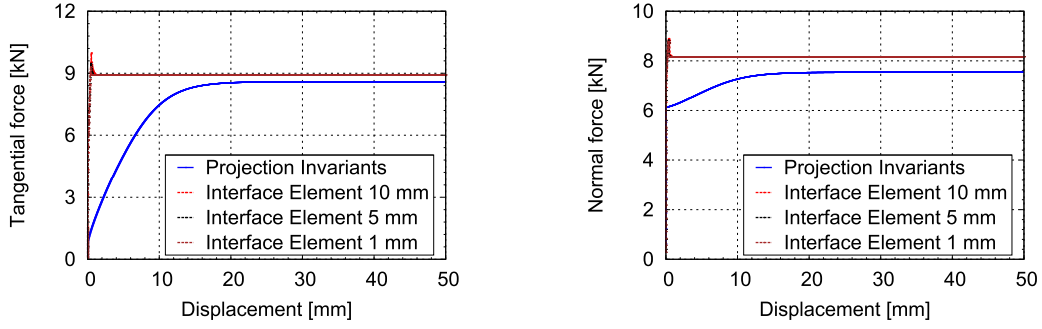


Figure 10: Comparison of tangential (left) and normal force (right) versus sliding distance at a constant pressure of  $100 = \text{kN/m}^2$

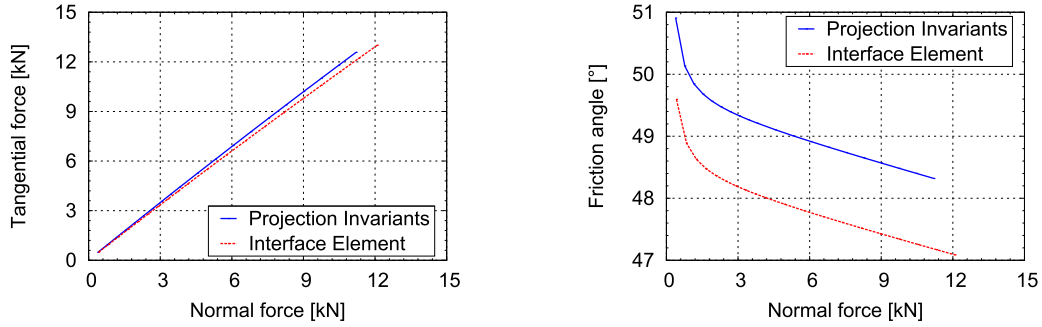


Figure 11: Comparison of tangential force (left) and friction angle (right) versus normal force

is the reduction of the CPU time with a factor of 10 compared to the corresponding computation of the continuum model. As a final remark, all computations of the contact case are conducted with the parameter  $\delta_T = 0.01 \text{ m}$  in (44).

**Remark:** Comparing the tangential force distribution of the projected contact formulation (figure 10) with the outcome of a triaxial test (figure 12) the results are qualitatively pretty close. The accordance can be explained with the similar evolution of the hardening parameters in both cases which is different to the corresponding behavior in a direct shear test. Looking at the normal-tangential force distribution of figure 11 the cap structure of the underlying yield criterion cannot be reproduced. The projected slip rule (46) and the yield criterion (27) have four roots on the axis of the normal force and on the space diagonal, respectively. However the domain is only defined between the inner two roots. Hence for values beyond the inner roots a unique back-projection onto the slip line can not be guaranteed anymore. A detailed explanation of these implications can be found in [20].

## 5 Projection based on a stress dependent coefficient of friction

Many frictional contact models are based directly on Coulomb's law where the specific slip behavior is included within the coefficient of friction leading to a function of  $\mu$  that depends for instance on the temperature, the pressure, the contact velocity or the surface roughness. A model based on a pressure and velocity dependent coefficient of friction can be found in [45] and a model for  $\mu$  designed for soil-structure interactions is formulated in [3] which introduces many new material parameters. More detailed

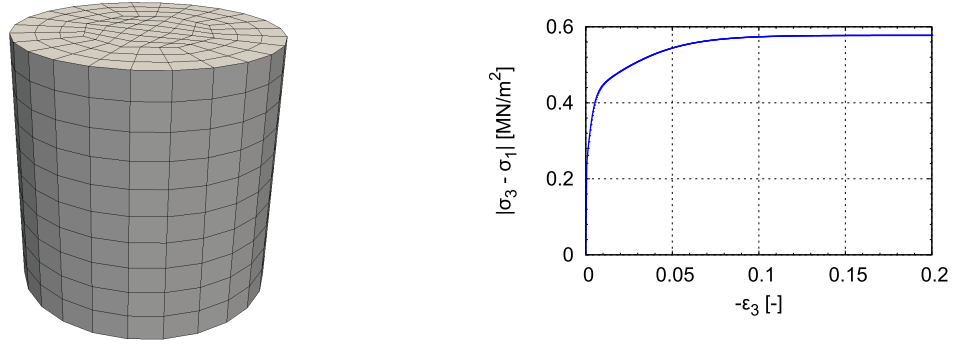


Figure 12: Finite element mesh of the triaxial test (left) and corresponding shear stress (right) during loading in vertical direction with a cell pressure of  $100 \text{ kN/m}^2$

descriptions of different frictional formulations can be found in [16] and the references therein. Based on this idea a new concept of projecting plasticity models onto the contact surface is developed so that the coefficient of friction and the also the normal contact stress depend directly on the 3-dimensional stress tensor. The formulations are set up exemplary using the Mortar method, as described in section 2, but can also applied to all kinds of contact formulations and solution methods. Coulomb's slip rule modifies then to

$$f^c = \|\bar{\mathbf{t}}_{TA n+1}\| + \mu(\boldsymbol{\sigma}_{A n+1}) \bar{t}_N(\boldsymbol{\sigma}_{A n+1}) = 0. \quad (54)$$

### 5.1 Projection scheme

As mentioned in the previous section contact can also be considered as shearing with load on top (figure 13). Instead of relating the continuum stress invariants to the contact stress as described in section 4



Figure 13: Equivalence of sliding and shear

the continuum kinematics are now expressed in terms of the contact quantities. In the case of a penalty regularization the tangential stress

$$\bar{\mathbf{t}}_{TA n+1} = -c_T [\bar{\mathbf{g}}_{TA n+1} - \bar{\mathbf{g}}_{TA n+1}^p] \quad (55)$$

is given by the difference of the actual and the plastic slip distance multiplied by a penalty parameter. In standard contact algorithms the actual slip distance is computed by an integration of the slip velocity over time. Mostly the finite difference method is applied and the actual slip distance follows as the sum of the previous slip distance and the actual increment

$$\bar{\mathbf{g}}_{TA n+1} = \int_{t_0}^{t_{n+1}} \dot{\bar{\mathbf{g}}}_T d\tau = [\bar{\mathbf{g}}_{TA n+1} - \bar{\mathbf{g}}_{TA n+1}^o] + \bar{\mathbf{g}}_{TA n}. \quad (56)$$

where  $\bar{\mathbf{g}}_{TAn+1}^o$  is the tangential distance of the previous integration point, see also equation (16). The tangential penalty parameter can be chosen arbitrarily and hence it can also be assumed to depend on twice the shear modulus  $\mu$  divided by an intrinsic virtual height. If the height approaches zero the penalty parameter approaches infinity which verifies the proposed approach. The actual tangential contact stress can now be reformulated

$$\bar{\mathbf{t}}_{TAn+1} = -2\mu \frac{1}{h} [\bar{\mathbf{g}}_{TAn+1} - \bar{\mathbf{g}}_{TAn+1}^p], \quad c_T = \frac{2\mu}{h}. \quad (57)$$

The second term corresponds exactly to the negative shear strain of the contact layer, see also figure 13.

$$\varepsilon_{3\alpha An+1} = \frac{1}{h \bar{a}_{An+1}} [(\bar{g}_{T\alpha An+1} - \bar{g}_{T\alpha An+1}^o) + \bar{g}_{T\alpha An}] \quad (58)$$

Since the Mortar method is used the tangential sliding has also to be divided by the area (45) of the slave node  $A$ . The negative sign of the tangential gap values in (57) can also be explained by means of a different direction of the difference vector in the case of contact compared to the shell theory, see [20] for more details. At the contact layer the membrane strain is assumed to be zero which follows also directly from the connection between contact and shell theory [20]

$$\varepsilon_{\alpha\beta An+1} \equiv 0. \quad (59)$$

As mentioned in section 4, the dilatancy effects can not be reproduced directly within a contact formulation and an alternative form has to be used. However the normal stress resulting from the enforcement of the non penetration condition which is here the Lagrange multiplier has to be equal to the normal stress at the contact layer

$$\sigma_{33An+1} = \bar{\lambda}_{NAn+1}. \quad (60)$$

Using a linear elastic stress strain relationship the elastic strain in the normal direction can be reformulated in terms of the Lagrange multiplier and the elastic normal strains

$$\varepsilon_{33An+1}^e = \frac{\sigma_{33An+1}}{\lambda + 2\mu} + \frac{\lambda}{\lambda + 2\mu} [\varepsilon_{11An+1}^e + \varepsilon_{22An+1}^e] \quad (61)$$

where the elastic normal strains are exactly the negative of its plastic counterpart. The stress strain relationship modifies in Voigt notation to

$$\tilde{\boldsymbol{\sigma}}_{An+1} = \begin{bmatrix} \sigma_{11An+1} \\ \sigma_{22An+1} \\ \sigma_{12An+1} \\ \sigma_{23An+1} \\ \sigma_{13An+1} \end{bmatrix} = \begin{bmatrix} c_{11} & c_{22} & 0 & 0 & 0 \\ c_{22} & c_{11} & 0 & 0 & 0 \\ 0 & 0 & \mu & 0 & 0 \\ 0 & 0 & 0 & \mu & 0 \\ 0 & 0 & 0 & 0 & \mu \end{bmatrix} \begin{bmatrix} \varepsilon_{11An+1}^e \\ \varepsilon_{22An+1}^e \\ 2\varepsilon_{12An+1}^e \\ 2\varepsilon_{23An+1}^e \\ 2\varepsilon_{13An+1}^e \end{bmatrix} + \begin{bmatrix} 1 \\ 1 \\ 0 \\ 0 \\ 0 \end{bmatrix} c_{33} \bar{\lambda}_{NAn+1}. \quad (62)$$

The new coefficients in (62) can be derived directly from equation (61)

$$c_{11} = \frac{2\lambda^2 + 4\lambda\mu + 4\mu^2}{\lambda + 2\mu}, \quad c_{22} = \frac{2\lambda^2 + 2\lambda\mu}{\lambda + 2\mu}, \quad c_{33} = \frac{\lambda}{\lambda + 2\mu} \quad (63)$$

Together with the nodal plastic strain at the previous time step all quantities are known and can be used within a 3-dimensional plasticity routine delivering the actual continuum stress and the material tangent at that contact node. Due to the known normal stress component the 3-dimensional material routine has to be modified slightly, but the solution algorithm remains the same. The final step in the

overall algorithm is the computation of the nodal coefficient of friction. Based on the analogy of the Coulomb friction law and the Mohr-Coulomb yield criterion (35) the coefficient of friction

$$\mu_{A n+1} = \left| \tan \left( \arcsin \left( \frac{\sqrt{\Pi_{s A n+1}} \cos \Theta_{A n+1}}{\frac{1}{3} \mathbf{I}_{\sigma A n+1} - \sqrt{\frac{\Pi_{s A n+1}}{3}} \sin \Theta_{A n+1}} \right) \right) \right| \quad (64)$$

as well as the normal stress component follows directly from the invariants of the actual stress tensor

$$\bar{t}_{N A n+1} = \frac{1}{3} \mathbf{I}_{\sigma A n+1} - \sqrt{\frac{\Pi_{s A n+1}}{3}} \sin \Theta_{A n+1}. \quad (65)$$

In an elastic response of the underlying 3-dimensional soil model the coefficient of friction is assigned as zero. Now the standard return mapping algorithm for Coulomb's law can be applied, see [16] for more details. Formulating the trial value analogous to (43) the actual tangential stress can be computed directly in dependence of Coulomb's slip rule together with the actual coefficient of friction

$$\begin{aligned} \text{stick : } \bar{\mathbf{t}}_{T A n+1} &= \bar{\mathbf{t}}_{T A n+1}^{tr} & \text{if } \mu_{A n+1} &= 0 \\ \text{slip : } \bar{\mathbf{t}}_{T A n+1} &= \mu_{A n+1} |\bar{t}_{N A n+1}| \frac{\bar{\mathbf{t}}_{T A n+1}^{tr}}{\|\bar{\mathbf{t}}_{T A n+1}^{tr}\|} & \text{if } \mu_{A n+1} &\neq 0. \end{aligned} \quad (66)$$

As a remark, the computation of the 3-dimensional stress can also be used to compute the missing Lode angle within the projection scheme of section 4.

## 5.2 Projection of Ehlers soil model

Since the normal stress component is already known within the computation of the virtual 3-dimensional stress at the contact layer only the residuum of the stress vector has to be modified within the solution algorithm of the pure continuum case

$$\mathbf{R}_{n+1} = \begin{bmatrix} \tilde{\boldsymbol{\sigma}}_{A n+1} - \tilde{\mathbf{D}}_e \left[ \boldsymbol{\varepsilon}_{A n+1}^{tr} - \gamma_{A n+1} \frac{\partial g_{n+1}}{\partial \boldsymbol{\sigma}_{A n+1}} \right] - c_{33} \bar{\lambda}_{N A n+1} \\ \mathbf{h}_{A n+1} - \mathbf{h}_{A n} - \gamma_{A n+1} \mathbf{g}_{A n+1}^h \\ f(\boldsymbol{\sigma}_{A n+1}, \mathbf{h}_{A n+1}) \end{bmatrix} = 0 \quad (67)$$

where  $\tilde{\mathbf{D}}_e$  is the modified elastic tangent given in (62). For the computation of the hardening values

$$\mathbf{g}_{A n+1}^h = (\mathbf{h}_{max} - \mathbf{h}_{A n+1}) \left[ \mathbf{C}_h^v \tan \nu_{A n+1}^p + \mathbf{C}_h^d \right] \left\| \frac{\partial g_{n+1}}{\partial \boldsymbol{\sigma}_{A n+1}} - \frac{1}{3} \text{tr} \left( \frac{\partial g_{n+1}}{\partial \boldsymbol{\sigma}_{A n+1}} \right) \mathbf{1} \right\| \quad (68)$$

and for the yield surface the same relations as for the continuum case can be used. Only the stress consists now of two parts  $\boldsymbol{\sigma}_{A n+1} = \boldsymbol{\sigma}(\tilde{\boldsymbol{\sigma}}_{A n+1}, \bar{\lambda}_{N A n+1})$ .

## 5.3 Numerical direct shear test

For the evaluation of the second projection scheme the same investigations using the same direct shear test as in section 4.3 are conducted. The height of the contact layer is assumed to consist of 10 mm

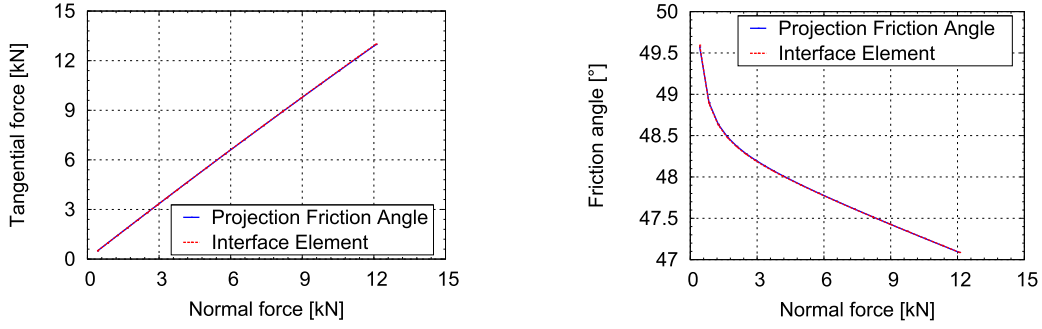


Figure 14: Comparison of tangential force (left) and friction angle (right) versus normal force

corresponding to 2-3 times the average grain diameter of GEBA fine sand. This height is imposed directly within the continuum simulation using standard elements at the interface and considered intrinsically within the projection scheme. Comparing the final tangential force and the final friction angle of different normal load levels (figure 14) both distribution shows the same outcome. The tangential force of the

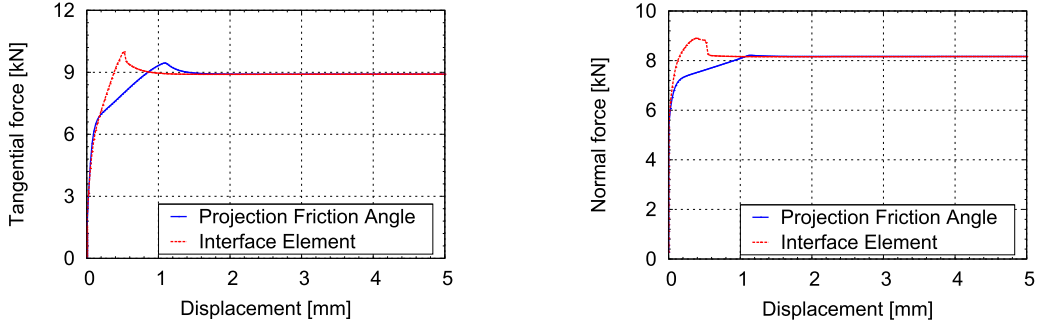


Figure 15: Comparison of tangential (left) and normal force (right) versus sliding distance of the first 5 mm at a constant pressure of  $100 = \text{kN/m}^2$  (right)

interface element and of the projected contact formulation end up both with the same force and shows a hardening peak (15). Only the height of the peak and the time when it occurs are different. The same holds for the normal force distribution (15). However replacing the upper specimen by a block of steel and comparing the distributions of the tangential and normal force both outcomes are almost equal (figure 16). The reason for the good accordance is the small normal strain in direction of sliding ( $\varepsilon_{11} \approx 10^{-6}$ ) due to the stiffer upper block which conforms to the assumption made in (59). In the soil-structure example this normal strain is around  $\varepsilon_{11} \approx 10^{-3}$  and can not be disregarded anymore. As well as for the projection scheme in section 4 the CPU time of this projection method is also around 10 times less as for the pure continuum case with interface elements in between of the upper and lower specimen.

## 6 Conclusion

In this work two different projection methods were developed each able to integrate plasticity models into a contact formulation. The first concept exploits the natural relation between Coulomb slip rule and

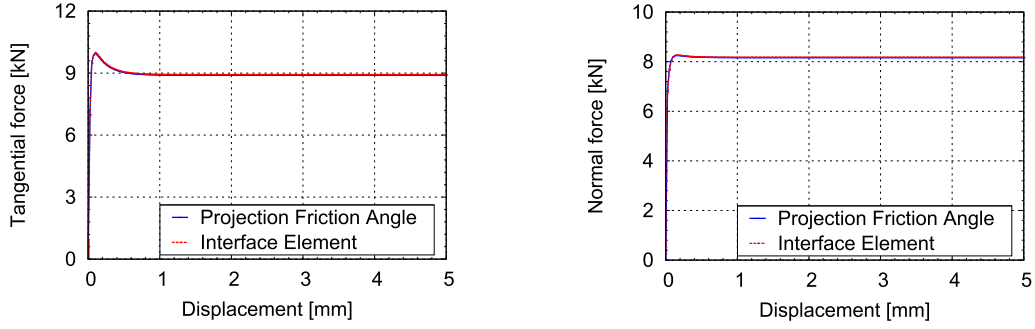


Figure 16: Comparison of tangential force (left) and normal force (right) versus sliding distance of the first 3 mm and at a constant pressure of  $100 = \text{kN/m}^2$  (right)

$\lambda = 100 \frac{\text{MN}}{\text{m}^2}$	$\mu = 150 \frac{\text{MN}}{\text{m}^2}$	$n_0^s = 0.585$	$n_{max}^s = 0.595$
$\beta_0 = 0.105$	$\beta_{max} = 0.263$	$C_\beta^v = -58$	$C_\beta^d = 350$
$\gamma_0 = 0.0$	$\gamma_{max} = 1.6$	$C_\gamma^v = -10$	$C_\gamma^d = 35$
$\delta_0 = 0.01 \frac{\text{m}^2}{\text{MN}}$	$\delta_{max} = 0.005 \frac{\text{m}^2}{\text{MN}}$	$C_\delta^v = 90$	$C_\delta^d = -15.9$
$\epsilon_0 = 0.0805 \frac{\text{m}^2}{\text{MN}}$	$\epsilon_{max} = 0.008 \frac{\text{m}^2}{\text{MN}}$	$C_\epsilon^v = -300$	$C_\epsilon^d = 300$
$\alpha = 0.01$	$\kappa = 0.0001 \frac{\text{MN}}{\text{m}^2}$	$m = 0.5454$	$\eta = 0.005$
$\Psi_1 = 0.97$	$\Psi_2 = 0.48$		

Table 1: Material data for GEBA sand

Mohr-Coulomb yield criterion to establish a connection between the stress invariants of the continuum and the contact quantities normal pressure and norm of the tangential stress. To model dilatancy effects properly a new dilatancy stress component was introduced that is able to consider a normal back-projection in the return mapping algorithm. Since the Lode angle is not zero in the case of dilatancy or contractancy effects, the first projection scheme underpredicts the real stress at the contact surface. If both bodies are sticking together the response behavior is only elastic. However in the continuum case a plastic response is also possible if the relative movement of the two bodies is only small. Both phenomena reason the slightly different outcome of the first projection concepts compared to the interface element.

The second projection concept has the advantage of a direct implementation of the plasticity model into the friction equations and constitutes a very robust algorithm. On the other hand the introduced height of the contact layer leads to an additional parameter which has to be determined. Since within soil-structure interactions the height of the contact layer corresponds to the height of a forced localization, a value of 2-3 times the average grain diameter is a reasonable approach. As shown in the results of the direct shear test, if the two specimens in contact are stiff enough that only very small membrane strains

occur, this projection scheme can reproduce the continuum behavior almost exact.

Additionally, as can be seen from the examples, the outcome of the triaxial test differs from the corresponding distribution of the direct shear test using the Ehlers soil model. The back-projection algorithm can also not deliver feasible results, if the normal pressure is too large or too small due to the double roots at the limits of the slip line.

In this work both projection concepts were applied only to soil-structure interactions, but they can be seen as a generic scheme able to describe all different kinds of contact phenomena. The modeling process of contact cases where the temperature has to be considered, like the heat transfer or the frictional heating, can be improved by this methods. Using a proper fluid description also lubrication effects can be modeled by this schemes to name only a view possible applications. Another advantage of this methods is that they can be used with all different kinds of contact formulations and solution methods.

**Acknowledgements** This research project is supported by the *Deutsche Forschungsgemeinschaft* (German Research Foundation) within the research unit 1136: Simulation of Geotechnical Construction Processes with Holistic Consideration of Constitutive Laws in Soils.

## References

- [1] I. Anastasopoulos and G. Gazetas. Foundation-structure systems over a rupturing normal fault: Part II. Analysis of the Kocaeli case histories. *Bulletin Earthquake Engineering*, 5:277–301, 2007.
- [2] S. Casciati and R.I. Borja. Dynamic FE analysis of South Memnon Colossus including 3D soil-foundation-structure interaction. *Computers and Structures*, 82:1719–1736, 2004.
- [3] A. Haraldsson. *Formulierung und Simulation der Kontaktvorgänge in der Baugrund-Tragwerk-Interaktion*. PhD thesis, Universität Hannover, Germany, 2003.
- [4] J.G. Potyondy. Skin friction between various soils and construction materials. *Géotechnique*, 11:339–353, 1961.
- [5] O. Reul. *In-situ Messungen und numerische Studien zum Tragverhalten der kombinierten Pfahl-Plattengründungen*. PhD thesis, Technischen Hochschule Darmstadt, Germany, 2000.
- [6] M. Uesugi, H. Kishida, and Y. Uchikawa. Friction between dry sand and concrete under monotonic and repeated loading. *Soils and Foundations*, 30:115–128, 1990.
- [7] C.S. Desai. Numerical design-analysis for piles in sands. *Journal of the Geotechnical Engineering Division*, GT6:613–635, 1974.
- [8] M.M. Zaman, C.S. Desai, and E.C. Drumm. Interface model for dynamic soil-structure interaction. *Journal of the Geotechnical Engineering*, 110:1257–1273, 1984.
- [9] R.E. Goodman, R.L. Taylor, and T.L. Brekke. A model for the mechanics of jointed rock. *Journal of the Soil Mechanics and Foundation Division*, 94:637–659, 1968.
- [10] J. Ghaboussi, E.L. Wilson, and J. Isenberg. Finite element for rock joints and interfaces. *Journal of the Soil Mechanics and Foundations Division*, 10:833–848, 1973.
- [11] S. Kucharski, T. Klimczak, A. Polijaniuk, and J. Kaczmarek. Finite-elements model for the contact of rough surfaces. *Wear*, 177:1–13, 1994.
- [12] L. Pei, S. Hyun, J.F. Molinari, and M.O. Robbins. Finite element modeling of elasto-plastic contact between rough surfaces. *Journal of the Mechanics and Physics of Solids*, 53:2385–2409, 2005.
- [13] C. S. Desai and H.J. Siriwardane. *Constitutive Laws for Engineering Materials with Emphasis on Geologic Materials*. Prentice-Hall, Englewood Cliffs, 1984.
- [14] A. Curnier. A theory of friction. *International Journal of Solids and Structures*, 20:637–647, 1984.
- [15] R. Michalowski and Z. Mroz. Associated and non-associated sliding rules in contact friction problems. *Archieve of Mechanics*, 30:259–276, 1978.
- [16] P. Wriggers. *Computational Contact Mechanics*. Springer-Verlag, Berlin, Heidelberg, 2<sup>nd</sup> edition, 2006.
- [17] J. Tejchman and W. Wu. Experimental and numerical study of sand-steel interfaces. *International Journal for Numerical and Analytical Methods in Geomechanics*, 19:513–536, 1995.
- [18] L.Hu and J. Pu. Testing and modeling of soil-structure interfaces. *Journal of Geotechnical and Geoenvironmental Engineering*, 130:851–860, 2004.
- [19] F.B. Belgacem, P. Hild, and P. Laborde. The mortar finite element method for contact problems. *Mathematical and Computational Modelling*, 28:263–271, 1998.

- 
- [20] C. Weißenfels. *Contact methods integrating plasticity models with application to soil mechanics*. PhD thesis, Universität Hannover, Germany, 2013.
- [21] P. Alart and A. Curnier. A mixed formulation for frictional contact problems prone to Newton like solution methods. *Computer Methods in Applied Mechanics and Engineering*, 92:353–375, 1991.
- [22] S. Hübner and B.I. Wohlmuth. A primal-dual active set strategy for nonlinear multibody contact problems. *Computer Methods in Applied Mechanics and Engineering*, 194:3147–3166, 2005.
- [23] W. Ehlers. A single-surface yield function for geomaterials. *Archive of Applied Mechanics*, 65:246–259, 1995.
- [24] W. Ehlers and B. Scholz. An inverse algorithm for the identification and the sensitivity analysis of the parameters governing micropolar elasto-plastic granular material. *Archive of Applied Mechanics*, 77:911–931, 2007.
- [25] J. O. Hallquist. Nike2d: An implicit, finite-deformation, finite element code for analyzing the static and dynamic response of two dimensional solids. Technical report, UCRL-52678, University of California, Lawrence Livermore National Laboratory, 1979.
- [26] T. A. Laursen. *Computational Contact and Impact Mechanics*. Springer-Verlag, Berlin, Heidelberg, 2006.
- [27] O.C. Zienkiewicz and R.L. Taylor. *The Finite Element Method*, volume Volume 1. McGraw Hill, London, 4<sup>rd</sup> edition, 1989.
- [28] P. Wriggers. *Nonlinear Finite Element Methods*. Springer-Verlag, Berlin, Heidelberg, 2008.
- [29] S. Hübner, G. Stadler, and B.I. Wohlmuth. A primal-dual active set algorithm for three-dimensional contact problems with coulomb friction. *SIAM Journal on Scientific Computing*, 30:572–596, 2008.
- [30] M.A. Puso and T.A. Laursen. A mortar segment-to-segment frictional contact method for large deformations. *Computer Methods in Applied Mechanics and Engineering*, 193:4891–4913, 2004.
- [31] A. Popp, M. Gitterle, M.W. Gee, and W.A. Wall. Finite deformation frictional mortar contact using a semi-smooth Newton method with consistent linearization. *International Journal for Numerical Methods in Engineering*, 84:543–571, 2010.
- [32] C. Bernardi, N. Debit, and Y. Maday. Coupling finite elements and spectral methods: First results. *Mathematics of Computation*, 54:21–39, 1990.
- [33] C. Bernardi, Y. Maday, and A.T. Patera. A new nonconforming approach to domain decomposition: The mortar element method. In H. Brezia and J.L. Lions, editors, *Nonlinear Partial Differential Equations and their Applications*, pages 13–51. Pitman: London, Wiley: New York, 1992.
- [34] M.A. Puso. A 3D mortar method for solid mechanics. *International Journal for Numerical Methods in Engineering*, 59:315–336, 2004.
- [35] M. Tur, F.J. Fuenmayor, and P. Wriggers. A mortar-based frictional contact formulation for large deformations using Lagrange multipliers. *Computer Methods in Applied Mechanics and Engineering*, 198:2860–2873, 2009.
- [36] B. Yang, T.A. Laursen, and X. Meng. Two dimensional mortar contact methods for large deformation frictional sliding. *International Journal for Numerical Methods in Engineering*, 62:1183–1225, 2005.
- [37] N. El-Abbasi and K.-J. Bathe. Stability and patch test performance of contact discretizations and a new solution algorithm. *Computers & Structures*, 79:1473–1486, 2001.

- 
- [38] M. Cyrus and J. Beck. Generalized two- and three-dimensional clipping. *Computers & Graphics*, 3:23–28, 1978.
- [39] J.C. Simo and R.L. Taylor. Consistent tangent operators for rate-independent elastoplasticity. *Computer Methods in Applied Mechanics and Engineering*, 48:101–118, 1985.
- [40] B. Scholz. *Application of a Micropolar Model to the Localization Phenomena in Granular Materials: General Model, Sensitivity Analysis and Parameter Optimization*. PhD thesis, Universität Stuttgart, Germany, 2007.
- [41] S.W. Sloan. Substepping schemes for the numerical integration of elastoplastic stress-strain relations. *International Journal for Numerical Methods in Engineering*, 24:893–911, 1987.
- [42] A. Perez-Foguet, A. Rodriguez-Ferran, and A. Huerta. Consistent tangent matrices for substepping schemes. *Computer Methods in Applied Mechanics and Engineering*, 190:4627–4647, 2001.
- [43] G. Duvaut and J.L. Lions. *Inequalities in Mechanics and Physics*. Springer-Verlag, Berlin, Heidelberg, 1976.
- [44] J.C. Simo. *Numerical Analysis and Simulation of Plasticity*. Handbook of Numerical Analysis VI. Elsevier Science B.V., 1998.
- [45] P. Wriggers and J. Reinelt. Multi-scale approach for frictional contact of elastomers on rough rigid surfaces. *Computer Methods in Applied Mechanics and Engineering*, 198:1996–2008, 2009.